Van der Waals Epitaxial Growth and High-Temperature Ferrimagnetism in Ultrathin Crystalline Magnetite (Fe_3O_4) Nanosheets

Yunzhou Xue,[‖,]* Hongtao Liu,[‖] Yi Zhang, Shenghuang Lin, Shu Ping Lau*

ABSTRACT: Two-dimensional (2D) magnets have attracted great research interest since long-range ferromagnetic ordering has been found in few-layer $Cr_2Ge_2Te_6$ and monolayer CrI_3. However, most 2D magnets have low magnetic ordering temperatures, impeding practical applications. Room-temperature or high-temperature intrinsic 2D magnets are highly desired for fundamental research and applications. Here, we present the van der Waals epitaxial growth, structure characterization, and magnetic properties of ultrathin crystalline magnetite (Fe_3O_4) nanosheets. The Curie temperature of as-grown ultrathin Fe_3O_4 nanosheets (847 K) is as high as its bulk counterpart (858 K). Large and saturated anomalous Hall effect (AHE) is observed in individual ultrathin Fe_3O_4 nanosheets up to 400 K, the highest working temperature of our apparatus. The anomalous Hall resistance increases as the thickness of Fe_3O_4 nanosheets decrease to ~ 10 nm. Irrespective of the thickness, the Hall angle reaches a maximum at 250 K, and the anomalous Hall conductivity σ_{xy} and longitudinal conductivity σ_{xx} obey a power-law scaling behavior of $\sigma_{xy} \propto \sigma_{xx}^{1.3}$, which slightly deviates from the universal scaling relation ($\sigma_{xy} \propto \sigma_{xx}^{1.6}$). The high Curie temperature and high stability of Fe_3O_4 nanosheets make it a promising candidate for spintronics and Hall sensors, as well as a building block for various van der Waals heterostructures.

KEYWORDS: van der Waals epitaxy, magnetite, anomalous Hall effect, Curie temperature, 2D magnet

Mermin-Wagner theorem reveals that magnetism hardly survives in two-dimensional (2D) materials due to enhanced thermal fluctuations.[1] However, the discovery of ferromagnetism in few-layer and even monolayer van der Waals layered materials re-ignites interest in 2D magnets due to their crucial role in spin valves, magnetic tunneling junctions, and other spin electronics.[2,3] Power efficient and miniaturized devices such as sensors, memories can be fabricated based on 2D magnets.[4] However, most 2D magnets suffer low magnetic ordering temperature, air sensitivity, or instability.[4–6] For example, the Curie temperature (T_C) of monolayer CrI_3 and bilayer $Cr_2Ge_2Te_6$ are 45 and ~30 K, respectively, much lower than room temperature.[2,3] Besides, CrI_3 is highly air-sensitive and easily degrades in air.[3] Room-temperature ferromagnetism has been found in bulk magnets Fe_5GeTe_2 and 1T-$CrTe_2$, while their T_C decreases considerably after thinning down to 2D flakes (310 K (bulk) versus 280 K (thin) for Fe_5GeTe_2, 310 K (bulk) versus 200 K (monolayer) for 1T-$CrTe_2$).[7–11] Room-temperature 2D ferromagnetism has been reported in monolayer Fe_3GeTe_2 as well.[12] However, its room-temperature ferromagnetism can only be realized by gate tuning. Hence, room-temperature or high-temperature intrinsic 2D magnets are still rarely reported but very appealing for both fundamental research and technological applications.[4]

Magnetite (Fe_3O_4) is one of the oldest magnetic materials with high T_C (858 K) and high spin polarization at room temperature. It has the inverse spinel structure, in which oxygen ions form a close-packed face-centered-cubic structure, and ferric ions (Fe^{3+})

and ferrous ions (Fe^{2+}) occupy the interstices.[13] One-eighth of the tetrahedral interstices (A-site) are occupied by Fe^{3+} ions. One-half of the octahedral interstices (B-site) are filled by equal amounts of Fe^{2+} and Fe^{3+} ions.[14] The spin moments of all the Fe^{3+} and Fe^{2+} ions within each sublattice are ferromagnetically aligned. However, the spins of Fe^{3+} ions are antiferromagnetically aligned between A- and B-sites and cancel out each other.[13] Only spins of Fe^{2+} ions in the B-sites contribute to the magnetization with the net magnetic moment of $2S = 2 \times 2 = 4\mu_B$ per formula unit.[13] Therefore, Fe_3O_4 is a ferrimagnet with a non-layered structure, making high-temperature magnetism possible in ultrathin nanoflakes. The hopping electrons between Fe^{2+} and Fe^{3+} ions in neighboring B-sites result in high conductivity around room temperature.[13] Upon cooling, the conductivity of the stoichiometric Fe_3O_4 suddenly drops at about 120 K, known as the Verwey transition due to charge ordering, along with a structural transition from cubic to a monoclinic structure.[13,15,16] The phase transition temperature (T_V) and the magnitude of the resistivity change are susceptible to the Fe/O ratio.[13,15]

Its high conductivity makes it possible to investigate the magnetism in individual ultrathin Fe_3O_4 nanosheets through the anomalous Hall effect (AHE). Meanwhile, it also provides a vital platform for exploring the AHE. The AHE is an additional phenomenon typically occurring in ferromagnets, which depends on the magnetization: $\rho_{xy} = R_0\mu_0 H + R_s\mu_0 M$, where ρ_{xy} is the Hall resistivity, H is the magnetic field, M is the magnetization, R_0 is the ordinary Hall coefficients, and R_s is the anomalous Hall coefficients. The ordinary Hall effect arises from the Lorentz force,

while the origin of the AHE remains controversial.[17] Based on the scaling relation between the anomalous Hall conductivity σ_{xy} and the longitudinal conductivity σ_{xx}, a unified theory with three regimes has been developed, which include the ultraclean limit with extremely high conductivity ($\sigma_{xy} \propto \sigma_{xx}$), the intrinsic intermediate regime ($\sigma_{xy} \sim$ constant), and the dirty limit with lower conductivity ($\sigma_{xy} \propto \sigma_{xx}^{1.6}$).[18,19] To the best of our knowledge, only the scaling behavior of $\sigma_{xy} \propto \sigma_{xx}^{1.6}$ is found in Fe_3O_4.[20,21] Other scaling relations have not been reported. High-quality ultrathin 2D Fe_3O_4 nanosheets will provide not only high-temperature ferrimagnetism for technological applications but also a platform for fundamental research. Hence, the growth and magnetic properties of individual ultrathin 2D Fe_3O_4 nanosheets are highly desired.

Here we report the van der Waals epitaxial growth of ultrathin crystalline Fe_3O_4 nanosheets on mica. The nanosheets were characterized by X-ray diffraction (XRD), Raman, and high-resolution transmission electron microscopy (HRTEM). Magnetization and electrical transport measurement demonstrated that as-grown ultrathin Fe_3O_4 nanosheets exhibit high T_C (847 K) and high-temperature intrinsic ferrimagnetism, comparable to high-quality bulk single crystals. The AHE is observed in individual Fe_3O_4 nanosheets with various thicknesses at temperatures up to 400 K, the highest working temperature of our apparatus. Moreover, the anomalous Hall resistance increases as the thickness of Fe_3O_4 nanosheets decrease to ~10 nm. Regardless of the thickness of the Fe_3O_4 nanosheets, the Hall angle reaches a maximum at 250 K, and the relationship between anomalous Hall conductivity σ_{xy} and

longitudinal conductivity σ_{xx} shows a power-law scaling relation of $\sigma_{xy} \propto \sigma_{xx}^{1.3}$. Fe_3O_4 nanosheets also show high stability in air demonstrated by Raman and transport measurement.

RESULTS AND DISCUSSION

Synthesis and Crystal Structure of Fe_3O_4 Nanosheets. Fe_3O_4 nanosheets were grown in a single-zone quartz tube furnace by a simple two-step method. Finely ground Fe_3O_4, NaCl, and KCl powder (200 mg) were first sintered at 750 ˚C for 30 min. Then the sintered mixture was used as the source, and freshly cleaved fluorophlogopite mica was used as the substrate, put above the sintered mixture with the freshly cleaved face downwards. Triangular- and truncated triangular-shaped Fe_3O_4 nanosheets were grown on mica in 30 min at 860 ˚C with 200 sccm Ar as carrier gas. As shown in Figures 1a, b, and S1, all the Fe_3O_4 nanosheets align well on mica and orient themselves within ±4 degrees of the dominant direction, demonstrating the characteristic of van der Waals epitaxial growth as the lattice of Fe_3O_4 is registered on the mica surface.

The quality of the as-grown Fe_3O_4 nanosheets was first investigated by micro-Raman spectroscopy, which provides a powerful tool to examine the quality of nanomaterials. Figure 1c shows the Raman spectrum of an as-grown Fe_3O_4 nanosheet. Four Raman peaks at 188, 309, 535, and 664 cm^{-1} can be observed and attributed to the $T_{2g}(1)$, E_g, $T_{2g}(2)$, and A_{1g} mode, respectively. These Raman peaks agree well with that of high-quality Fe_3O_4 single crystals.[22] Moreover, the Fe_3O_4 nanosheets show high

stability in air. No apparent change of their Raman spectra was observed after exposure to the air for more than two months, as shown in Figure S2. The A_{1g} mode Raman mapping of a Fe_3O_4 nanosheet is shown in Figure 1d. A quite uniform color contrast in the mapping indicates the uniform crystallinity of the nanosheet. As shown in Figure 1e, the atomic force microscopy (AFM) topological image of a Fe_3O_4 nanosheet displays its atomically flat surface and 7.9 nm thickness. XRD confirmed the crystalline nature of the Fe3O4 nanosheets at room temperature. Four sharp peaks are observed, as shown in Figure 1f, suggesting that the Fe_3O_4 nanosheets are high-quality crystals and highly oriented on mica with (111) facets parallel to the mica surface. The distance between (111) planes of Fe_3O_4 extracted from XRD is 4.808 Å, very close to that of a high-quality single crystal (4.852 Å, Magnetite, syn, PDF#19-0629), indicating no apparent strain is induced due to the weak van der Waals interactions between Fe_3O_4 nanosheets and mica.

The high-quality crystalline nature of as-grown Fe_3O_4 nanosheets was further confirmed by TEM. A low-magnification TEM image of a Fe_3O_4 nanosheet is shown in the inset in Figure 2a, which exhibits a regularly triangular shape. Its corresponding energy-dispersive X-ray spectroscopy (EDS) mapping images shown in Figure 2a, b exhibit uniform Fe and O distribution throughout the entire top surface. No elements of NaCl and KCl used during growth are observed on both the top surface and cross-section of the nanosheets (Figure S4). HRTEM image of one corner of the triangular Fe_3O_4 nanosheet in Figure 2a is shown in Figure 2c. The (111) facet is observed in the

top view image and is consistent with the XRD result. The high crystallinity of the nanosheet is further confirmed by selected area electron diffraction (SAED), which exhibits sharp diffraction spots as shown in Figure 2d. Moreover, the diffraction patterns collected at each corner of the triangular Fe_3O_4 nanosheet in Figure 1a are almost identical, as shown in Figure S3d-f, indicating its single-crystal nature. The cross-sectional image can also observe the (111) planes of the Fe_3O_4 nanosheet parallel to its surface (Figure 2e). The sharp diffraction spots of the cross-sectional Fe_3O_4 further demonstrate its high crystallinity, as shown in Figure 2f. The top surface and cross-sectional HRTEM images (Figure 2c, e) indicate that the Fe_3O_4 nanosheets are high-quality crystals and highly oriented on the mica with (111) facets parallel to the mica surface. No structural defects and antiphase boundaries are observed in all the examined nanosheets.[23]

Magnetic Properties of Fe_3O_4 Nanosheets. The magnetic properties of the as-grown Fe_3O_4 nanosheets were investigated by the Magnetic Property Measurement System (MPMS3, Quantum Design Inc.) in the temperature range of 2–900 K. Temperature-dependent magnetization was measured to determine the T_C, as well as the T_V, of the as-grown ultrathin Fe_3O_4 nanosheets. As shown in Figure 3a, the T_V of the ultrathin Fe_3O_4 nanosheets is 117 K, and the T_C can be identified at about 847 K by fitting the curve, the latter of which is slightly lower than that of bulk (858 K). It demonstrates that lowering the thickness of Fe_3O_4 crystals does not significantly reduce its T_C and high-temperature ferrimagnetism persists in ultrathin nanosheets.

Magnetization curves measured at various temperatures further support this result. As shown in Figure 3b, c, both in-plane and out-of-plane magnetization of the ultrathin Fe_3O_4 nanosheets were measured at temperatures from 100 to 400 K. In-plane and out-of-plane magnetic fields were applied parallel and perpendicular to the (111) plane of Fe_3O_4 nanosheets, respectively. The nanosheets are fully magnetized and saturated in a low field (~0.5 T in in-plane, ~1 T in out-of-plane). The ultrathin Fe_3O_4 nanosheets are easier magnetized in the in-plane field than in the out-of-plane field (Figures 3b, c and Figure S6), which agrees well with the high-quality Fe_3O_4 thin films magnetization behavior.[24] The saturation magnetizations slightly decrease both in in-plane and out-of-plane fields as temperature increases from 100 to 400 K (Figure 3b, c). Its saturation magnetization decreases rapidly when the temperature approaches T_C (Figure 3d). The fully saturated magnetization curves are in stark contrast to thin films grown by other methods, suggesting that antiphase boundaries in the as-grown Fe_3O_4 nanosheets are of low density. The high density of antiphase boundaries usually makes the magnetization curve hard to saturate.[25]

Magneto-transport Properties of Individual Fe_3O_4 Nanosheets. Magnetic properties of the individual Fe_3O_4 nanosheets with various thicknesses were investigated through magneto-transport measurements. As shown in Figure S7a, the temperature-dependent resistivity gradually increases upon cooling, and no apparent sudden increase is observed in all the studied samples, probably due to the slight nonstoichiometry of the samples.[13,20] However, the Verwey transition is still observed

as a kink in ultrathin samples (Figure S7a, b), consistent with the result measured by MPMS3 and the value of ultrathin Fe_3O_4 film.[26] The presence of the Verwey transition ascertains the high quality of the nanosheets. The linear part in the curves just around and above the T_V shown in Figure S7a demonstrates that charge transport is typically governed by thermally activated hopping (Table S1). Here we mainly focus on electrical transport properties above the T_V (150 – 400 K). The room temperature resistivity of the Fe_3O_4 nanosheets with various thicknesses is listed in Table S1, which are close to high-quality homogeneous Fe_3O_4 single crystal.[15]

Bulk-like Fe_3O_4 nanosheets (556 nm) exhibits similar magneto-transport behaviors to that of high-quality bulk Fe_3O_4 single crystals.[27–30] Out-of-plane and in-plane fields were applied perpendicular and parallel to the (111) plane of the Fe_3O_4 nanosheets, respectively. Positive magnetoresistance (MR) (Figure 4a) and negative MR (Figure S8b–d) are observed in the out-of-plane and in-plane fields, respectively. Positive MR is weakly dependent on the magnetic field when the field is higher than ~0.5 T, while negative MR is weakly dependent on temperature. Although the amplitude of positive MR decreases as temperature increases from 150 to 400 K, MR curves maintain a similar shape. As shown in Figure 4b, the AHE is observed in an out-of-plane field in the temperature range of 150 – 400 K. The perfect proportionality between Hall resistance and magnetization curves shown in Figure S9 demonstrates that the AHE in the Fe_3O_4 nanosheets is controlled by magnetization, consistent with the Karplus-Luttinger theory.[31]

For ultrathin Fe_3O_4 nanosheets (8.1–21 nm), the positive MR (Figure 4c, e and Figure S10c, 11c, 13c, 14c) are also weakly dependent on the field as that of bulk-like one, but in a slightly higher field of ~0.8 T. Moreover, butterfly-shaped hystereses are observed within the field of ±0.2 T in all the ultrathin nanosheets, which is different from the bulk-like Fe_3O_4 nanosheet and would be caused by spin switching.[32] The AHE is observed and persists up to 400 K, as shown in Figures S10d, 11d, 13d, 14d, and Figure 4d, f. In all the studied Fe_3O_4 nanosheets, the AHE dominates the Hall effect (Figure S16) and saturate at ~1 T, which is in stark contrast to Fe_3O_4 thin films. No signature of saturation is observed even in a field up to 9 T due to the large density of antiphase boundaries in the Fe_3O_4 thin films.[20] Additionally, as shown in Figure 5a, anomalous Hall resistance increases as the thickness decreases from 556 to 10.9 nm, and more than one order of magnitude increase in anomalous Hall resistance is observed in the ultrathin Fe_3O_4 nanosheets even at a temperature as high as 400 K. However, the decrease of anomalous Hall resistance in the 8.1 nm thick Fe_3O_4 nanosheet requires further study. The large anomalous Hall resistance in the ultrathin Fe_3O_4 nanosheets may be associated with their sizeable longitudinal resistance, as shown in Figure 5b and Figure S19. The anomalous Hall resistance and longitudinal resistance increase with descreaeing temperataure (Figures 5b and S19). However, the Hall angle ($\sigma_{xy}^{(0)}/\sigma_{xx}^{(0)}$) reaches a maximum at 250 K irrespective of thickness as shown in Figure 5c. The relationship of anomalous Hall conductivity σ_{xy} ($\sigma_{xy} = \frac{\rho_{xy}}{\rho_{xx}^2+\rho_{xy}^2}$) and longitudinal conductivity σ_{xx} ($\sigma_{xx} = \frac{\rho_{xx}}{\rho_{xx}^2+\rho_{xy}^2}$) is shown in Figure 5d. Despite different longitudinal resistance and anomalous Hall resistance for different nanosheets, a power-

law scaling relation $\sigma_{xy} \propto \sigma_{xx}^{1.3}$ is found, which slightly deviates from the universal scaling relation ($\sigma_{xy} \propto \sigma_{xx}^{1.6}$).[17,20,21] Though the scaling exponent is smaller in our Fe_3O_4 nanosheets, it is still close to the value in the disordered insulating regime with phonon-assisted hopping transport with the scaling exponent from 1.33 to 1.76.[33] However, the disorder in the Fe_3O_4 nanosheets cannot reach the dirty limit, which has a scaling exponent of 1.6.[19] It is probably due to the high quality of Fe_3O_4 nanosheets and low density of antiphase boundaries that lead to the smaller scaling exponent. Another probability is that the scaling relation in the Fe_3O_4 nanosheets lies in the crossover regime from the dirty limit to the intrinsic intermediate regime, and thus has a smaller value of the scaling exponent of 1.3.[18,19,34] The large, linear and saturated AHE in the ultrathin Fe_3O_4 nanosheets makes it a promising material for Hall sensors. More importantly, its high T_C makes it an excellent candidate for spintronics.

CONCLUSIONS

In summary, high-quality ultrathin Fe_3O_4 nanosheets have been epitaxially grown on mica with (111) plane as exposed facets. Magnetization measurement shows that the T_C of the ultrathin Fe_3O_4 nanosheets is as high as 847 K and the T_V is at 117 K. The AHE in the individual ultrathin nanosheets persist up to 400 K. The anomalous Hall resistance increases as the thickness of Fe_3O_4 nanosheets decrease from bulk-like to ~10 nm, probably due to the rise in longitudinal resistance. The anomalous Hall conductivity approximately scales with longitudinal conductivity as $\sigma_{xy} \propto \sigma_{xx}^{1.3}$ regardless of thickness and temperature. High-temperature ferrimagnetism and large

AHE, as well as its air stability, make it a promising candidate for spintronics and Hall sensors. All in all, it provides a versatile platform for investigating a wide range of spintronic phenomena, Verwey transition, the AHE, and other applications.

METHODS

CVD Growth of Fe_3O_4 nanosheets. A two-step method was used to grow Fe_3O_4 nanosheets. First, Fe_3O_4/NaCl/KCl (200 mg) powder with a mass ratio of 0.091/0.404/0.505 was ground by a mortar and put into a quartz boat as the Fe_3O_4 source. Next, it was sintered in a single heating zone furnace at 750 °C for 30 minutes with 200 sccm Ar as protection gas, then cooling down to room temperature. The sintered lump was used as a Fe_3O_4 source to grow bulk-like Fe_3O_4 nanosheets, while the sintered lump was sintered again at 860 °C for 10 min before growing ultrathin Fe_3O_4 nanosheets. To produce Fe_3O_4 nanosheets, freshly cleaved fluorophlogopite mica, as the growth substrate, was put above the sintered Fe_3O_4/NaCl/KCl lump with the freshly cleaved face downward. The quartz tube was evacuated for 10 min with a pump to remove the air, and then filled with Ar to ambient pressure before temperature ramping. The furnace was heated up to 860 °C in 35 minutes with 200 sccm Ar as carrier gas and held at 860 °C for 30 minutes. Followed by slowly cooling down to ~610 °C, the furnace cooled rapidly down to room temperature by opening its cover.

Device fabrication and electrical transport measurement. As-grown Fe_3O_4 nanosheets were first transferred from the growth substrate mica onto SiO_2/Si with the assistance of polystyrene.[35–37] Hall bar devices were fabricated by standard e-beam

lithography followed by deposition of 5 nm Cr and 60 nm Au as contact electrodes by thermal evaporation. All magneto-transport measurements were performed using a Physical Property Measurement System (Quantum Design Inc.). All the Hall and MR results were symmetrized using a standard symmetrization procedure.

Characterization. As-grown Fe_3O_4 nanosheets were characterized by AFM (Bruker NanoScope 8) operated in AC-mode, optical microscopy (Leica), Raman spectroscopy (Witec confocal Raman system) with laser wavelength of 514 nm and objective magnification of ×100, XRD (Empyrean 2.2 kW, target, Cu), TEM (JEM-3200FS, JEOL) at room temperature, and MPMS3.

ASSOCIATED CONTENT

Supporting information

The Supporting Information is available free of charge at https://pubs.acs.org/doi/10.1021/acsnano.XXXXXXX.

Optical images, Raman spectra, cross-sectional TEM image, in-plane and out-of-plane *M-H* curves, temperature-dependent resistivities, AFM images of the devices, in-plane MR of the 556 nm Fe_3O_4 nanosheet, MR and Hall of other thickness Fe_3O_4 nanosheets, MR and Hall of the 556 and 8.1 nm Fe_3O_4 nanosheets before and after exposure to air, relationship between anomalous Hall resistance and longitudinal resistance.

AUTHOR INFORMATION

Corresponding Authors

Yunzhou Xue − *College of Chemistry and Environmental Engineering, Shenzhen University, Shenzhen 518052, P.R. China;* orcid.org/0000-0002-2908-9032; Email:

xueyz@iccas.ac.cn

Shu Ping Lau − *Department of Applied Physics, The Hong Kong Polytechnic University, Hung Hom, Kowloon, Hong Kong, P.R. China;* orcid.org/0000-0002-5315-8472; Email: apsplau@polyu.edu.hk

Authors

Hongtao Liu − *Department of Physics, The Hong Kong University of Science and Technology, Clear Water Bay, Hong Kong, P.R. China;* orcid.org/0000-0003-0500-7204

Yi Zhang − *School of Physics, Sun Yat-Sen University, Guangzhou, 510275, P.R. China*

Shenghuang Lin − *Songshan Lake Materials Laboratory, Dongguan, Guangdong 523808, P.R. China*

Author Contributions

‖Y.X. and H.L. contributed equally.

Notes

The authors declare no competing financial interest.

ACKNOWLEDGMENTS

This work was financially supported by the Hong Kong Polytechnic University grant (1-ZVGH), the Research Grants Council of Hong Kong (AoE/P-701/20), the National Natural Science Foundation of China (Grant 61904113), and the Science and Technology Innovation Commission of Shenzhen (JCYJ20180305125616770).

REFERENCES

(1) Mermin, N. D.; Wagner, H. Absence of Ferromagnetism or Antiferromagnetism in One- or Two-Dimensional Isotropic Heisenberg Models. *Phys. Rev. Lett.* **1966**,

17, 1133–1136.

(2) Gong, C.; Li, L.; Li, Z.; Ji, H.; Stern, A.; Xia, Y.; Cao, T.; Bao, W.; Wang, C.; Wang, Y.; Qiu, Z. Q.; Cava, R. J.; Louie, S. G.; Xia, J.; Zhang, X. Discovery of Intrinsic Ferromagnetism in Two-Dimensional van Der Waals Crystals. *Nature* **2017**, *546*, 265–269.

(3) Huang, B.; Clark, G.; Navarro-Moratalla, E.; Klein, D. R.; Cheng, R.; Seyler, K. L.; Zhong, D.; Schmidgall, E.; McGuire, M. A.; Cobden, D. H.; Yao, W.; Xiao, D.; Jarillo-Herrero, P.; Xu, X. Layer-Dependent Ferromagnetism in a van Der Waals Crystal down to the Monolayer Limit. *Nature* **2017**, *546*, 270–273.

(4) Gong, C.; Zhang, X. Two-Dimensional Magnetic Crystals and Emergent Heterostructure Devices. *Science* **2019**, *363*, eaav4450.

(5) Wang, M.-C.; Huang, C.-C.; Cheung, C.-H.; Chen, C.-Y.; Tan, S. G.; Huang, T.-W.; Zhao, Y.; Zhao, Y.; Wu, G.; Feng, Y.-P.; Wu, H.-C.; Chang, C.-R. Prospects and Opportunities of 2D van Der Waals Magnetic Systems. *Ann. Phys.* **2020**, *532*, 1900452.

(6) Li, H.; Ruan, S.; Zeng, Y.-J. Intrinsic Van Der Waals Magnetic Materials from Bulk to the 2D Limit: New Frontiers of Spintronics. *Adv. Mater.* **2019**, *31*, 1900065.

(7) May, A. F.; Ovchinnikov, D.; Zheng, Q.; Hermann, R.; Calder, S.; Huang, B.; Fei, Z.; Liu, Y.; Xu, X.; McGuire, M. A. Ferromagnetism Near Room Temperature in the Cleavable van Der Waals Crystal Fe_5GeTe_2. *ACS Nano* **2019**, *13*, 4436–4442.

(8) Freitas, D. C.; Weht, R.; Sulpice, A.; Remenyi, G.; Strobel, P.; Gay, F.; Marcus, J.; Núñez-Regueiro, M. Ferromagnetism in Layered Metastable 1T-$CrTe_2$. *J. Phys. Condens. Matter* **2015**, *27*, 176002.

(9) Zhang, X.; Lu, Q.; Liu, W.; Niu, W.; Sun, J.; Cook, J.; Vaninger, M.; Miceli, P. F.; Singh, D. J.; Lian, S.-W.; Chang, T.-R.; He, X.; Du, J.; He, L.; Zhang, R.; Bian, G.; Xu, Y. Room-Temperature Intrinsic Ferromagnetism in Epitaxial $CrTe_2$ Ultrathin Films. *Nat. Commun.* **2021**, *12*, 2492.

(10) Meng, L.; Zhou, Z.; Xu, M.; Yang, S.; Si, K.; Liu, L.; Wang, X.; Jiang, H.; Li,

B.; Qin, P.; Zhang, P.; Wang, J.; Liu, Z.; Tang, P.; Ye, Y.; Zhou, W.; Bao, L.; Gao, H.-J.; Gong, Y. Anomalous Thickness Dependence of Curie Temperature in Air-Stable Two-Dimensional Ferromagnetic 1T-$CrTe_2$ Grown by Chemical Vapor Deposition. *Nat. Commun.* **2021**, *12*, 809.

(11) Sun, X.; Li, W.; Wang, X.; Sui, Q.; Zhang, T.; Wang, Z.; Liu, L.; Li, D.; Feng, S.; Zhong, S.; Wang, H.; Bouchiat, V.; Nunez Regueiro, M.; Rougemaille, N.; Coraux, J.; Purbawati, A.; Hadj-Azzem, A.; Wang, Z.; Dong, B.; Wu, X.; Yang, T.; Yu, G.; Wang, B.; Han, Z.; Han, X.; Zhang, Z. Room Temperature Ferromagnetism in Ultra-Thin van Der Waals Crystals of 1T-$CrTe_2$. *Nano Res.* **2020**, *13*, 3358–3363.

(12) Deng, Y.; Yu, Y.; Song, Y.; Zhang, J.; Wang, N. Z.; Sun, Z.; Yi, Y.; Wu, Y. Z.; Wu, S.; Zhu, J.; Wang, J.; Chen, X. H.; Zhang, Y. Gate-Tunable Room-Temperature Ferromagnetism in Two-Dimensional Fe_3GeTe_2. *Nature* **2018**, *563*, 94–99.

(13) Walz, F. The Verwey Transition - a Topical Review. *J. Phys. Condens. Matter* **2002**, *14*, R285–R340.

(14) Liu, X.; Mi, W. B. Structure, Magnetic and Transport Properties of Fe_3O_4 near Verwey Transition. *Acta Phys. Sin.* **2020**, *69*, 040505.

(15) Verwey, E. J. W. Electronic Conduction of Magnetite (Fe_3O_4) and Its Transition Point at Low Temperatures. *Nature* **1939**, *144*, 327–328.

(16) Senn, M. S.; Wright, J. P.; Attfield, J. P. Charge Order and Three-Site Distortions in the Verwey Structure of Magnetite. *Nature* **2012**, *481*, 173–176.

(17) Nagaosa, N.; Sinova, J.; Onoda, S.; MacDonald, A. H.; Ong, N. P. Anomalous Hall Effect. *Rev. Mod. Phys.* **2010**, *82*, 1539–1592.

(18) Onoda, S.; Sugimoto, N.; Nagaosa, N. Intrinsic Versus Extrinsic Anomalous Hall Effect in Ferromagnets. *Phys. Rev. Lett.* **2006**, *97*, 126602.

(19) Miyasato, T.; Abe, N.; Fujii, T.; Asamitsu, A.; Onoda, S.; Onose, Y.; Nagaosa, N.; Tokura, Y. Crossover Behavior of the Anomalous Hall Effect and Anomalous Nernst Effect in Itinerant Ferromagnets. *Phys. Rev. Lett.* **2007**, *99*, 086602.

(20) Fernández-Pacheco, A.; De Teresa, J. M.; Orna, J.; Morellon, L.; Algarabel, P.

A.; Pardo, J. A.; Ibarra, M. R. Universal Scaling of the Anomalous Hall Effect in Fe_3O_4 Epitaxial Thin Films. *Phys. Rev. B* **2008**, *77*, 100403.

(21) Venkateshvaran, D.; Kaiser, W.; Boger, A.; Althammer, M.; Rao, M. S. R.; Goennenwein, S. T. B.; Opel, M.; Gross, R. Anomalous Hall Effect in Magnetite: Universal Scaling Relation between Hall and Longitudinal Conductivity in Low-Conductivity Ferromagnets. *Phys. Rev. B* **2008**, *78*, 092405.

(22) Shebanova, O. N.; Lazor, P. Raman Spectroscopic Study of Magnetite ($FeFe_2O_4$): A New Assignment for the Vibrational Spectrum. *J. Solid State Chem.* **2003**, *174*, 424–430.

(23) Margulies, D. T.; Parker, F. T.; Rudee, M. L.; Spada, F. E.; Chapman, J. N.; Aitchison, P. R.; Berkowitz, A. E. Origin of the Anomalous Magnetic Behavior in Single Crystal Fe_3O_4 Films. *Phys. Rev. Lett.* **1997**, *79*, 5162–5165.

(24) Matsuzaki, K.; Lazarov, V. K.; Lari, L.; Hosono, H.; Susaki, T. Fe_3O_4(111) Thin Films with Bulk-like Properties: Growth and Atomic Characterization. *J. Phys. Appl. Phys.* **2012**, *46*, 022001.

(25) Bataille, A. M.; Ponson, L.; Gota, S.; Barbier, L.; Bonamy, D.; Gautier-Soyer, M.; Gatel, C.; Snoeck, E. Characterization of Antiphase Boundary Network in Fe_3O_4(111) Epitaxial Thin Films: Effect on Anomalous Magnetic Behavior. *Phys. Rev. B* **2006**, *74*, 155438.

(26) Reisinger, D.; Majewski, P.; Opel, M.; Alff, L.; Gross, R. Hall Effect, Magnetization, and Conductivity of Fe_3O_4 Epitaxial Thin Films. *Appl. Phys. Lett.* **2004**, *85*, 4980–4982.

(27) Shiozaki, I.; Hurd, C. M.; McAlister, S. P.; McKinnon, W. R.; Strobel, P. Galvanomagnetic Measurements in Fe_3O_4. *J. Phys. C Solid State Phys.* **1981**, *14*, 4641–4653.

(28) Liu, X. H.; Chang, C. F.; Tjeng, L. H.; Komarek, A. C.; Wirth, S. Large Magnetoresistance Effects in Fe_3O_4. *J. Phys. Condens. Matter* **2019**, *31*, 225803.

(29) Feng, J. S.-Y.; Pashley, R. D.; Nicolet, M.-A. Magnetoelectric Properties of Magnetite Thin Films. *J. Phys. C Solid State Phys.* **1975**, *8*, 1010–1022.

(30) Matsuzaki, K.; Hosono, H.; Susaki, T. Magnetotransport Properties across Verwey Transition in Fe_3O_4 (111) Epitaxial Thin Films. *Appl. Phys. Express* **2013**, *6*, 073009.

(31) Karplus, R.; Luttinger, J. M. Hall Effect in Ferromagnetics. *Phys. Rev.* **1954**, *95*, 1154–1160.

(32) Checkelsky, J. G.; Lee, M.; Morosan, E.; Cava, R. J.; Ong, N. P. Anomalous Hall Effect and Magnetoresistance in the Layered Ferromagnet $Fe_{1/4}TaS_2$: The Inelastic Regime. *Phys. Rev. B* **2008**, *77*, 014433.

(33) Liu, X.-J.; Liu, X.; Sinova, J. Scaling of the Anomalous Hall Effect in the Insulating Regime. *Phys. Rev. B* **2011**, *84*, 165304.

(34) Sangiao, S.; Morellon, L.; Simon, G.; De Teresa, J. M.; Pardo, J. A.; Arbiol, J.; Ibarra, M. R. Anomalous Hall Effect in Fe (001) Epitaxial Thin Films over a Wide Range in Conductivity. *Phys. Rev. B* **2009**, *79*, 014431.

(35) Gurarslan, A.; Yu, Y.; Su, L.; Yu, Y.; Suarez, F.; Yao, S.; Zhu, Y.; Ozturk, M.; Zhang, Y.; Cao, L. Surface-Energy-Assisted Perfect Transfer of Centimeter-Scale Monolayer and Few-Layer MoS_2 Films onto Arbitrary Substrates. *ACS Nano* **2014**, *8*, 11522–11528.

(36) Chen, S.; Liu, H.; Chen, F.; Zhou, K.; Xue, Y. Synthesis, Transfer, and Properties of Layered $FeTe_2$ Nanocrystals. *ACS Nano* **2020**, *14*, 11473–11481.

(37) Liu, H.; Xue, Y. Van Der Waals Epitaxial Growth and Phase Transition of Layered $FeSe_2$ Nanocrystals. *Adv. Mater.* **2021**, *33*, 2008456.

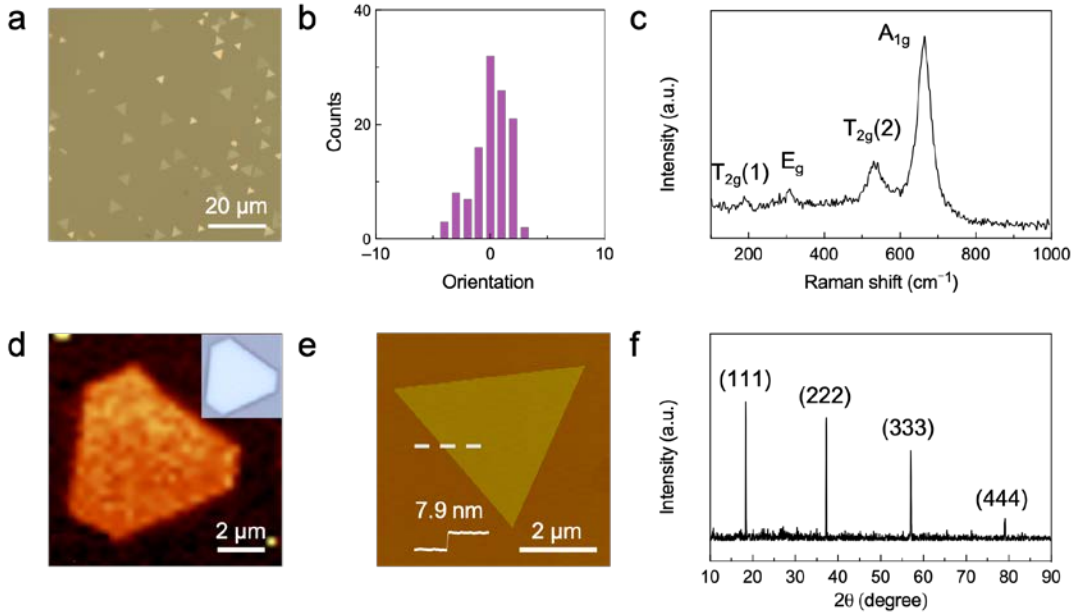

Figure 1. Van der Waals epitaxial growth of Fe_3O_4 nanosheets on mica substrate. (a) Optical image of ultrathin Fe_3O_4 nanosheets grown on mica. (b) Histogram of the orientation distribution of the Fe_3O_4 nanosheets on mica. (c) Raman spectrum of a Fe_3O_4 nanosheet with A_{1g}, $T_{2g}(2)$, E_g, $T_{2g}(1)$ modes located at 665, 535, 300, 194 cm^{-1}, respectively. (d) Raman mapping image based on the intensity of the 665 cm^{-1} peak of the Fe_3O_4 nanosheet with its optical image shown in the inset. (e) AFM image and height profile of a triangular Fe_3O_4 nanosheet with a thickness of 7.9 nm. (f) Room-temperature XRD pattern of the Fe_3O_4 nanosheets.

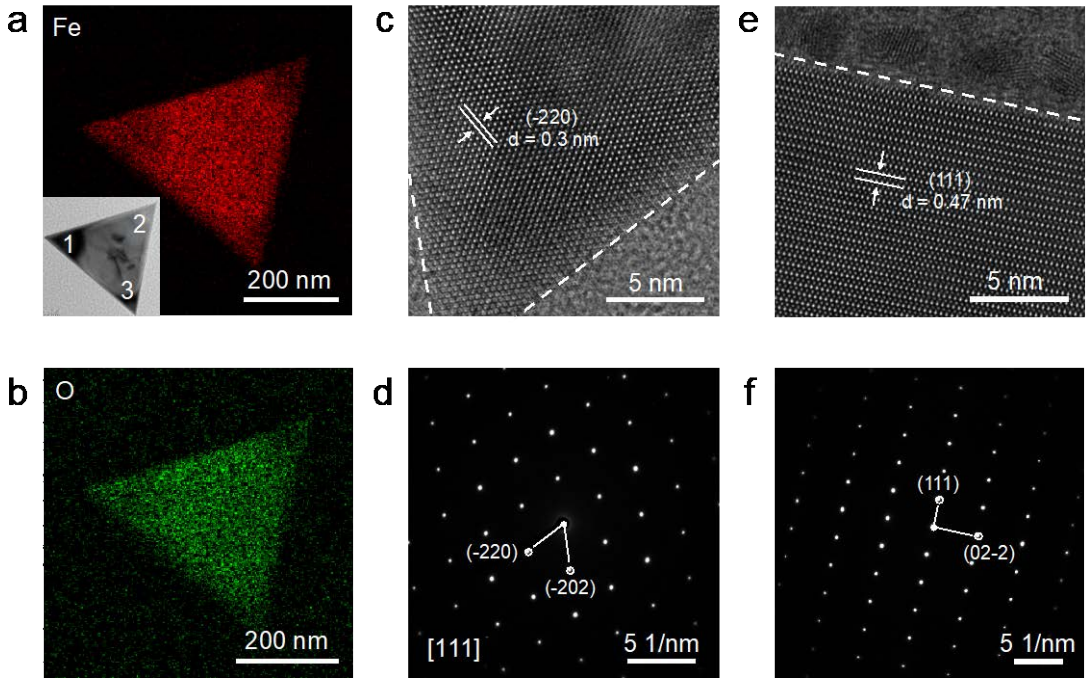

Figure 2. TEM characterization of as-grown Fe_3O_4 nanosheets. (a,b) EDS mapping of Fe (a) and O (b) of the Fe_3O_4 nanosheet with its low-magnification TEM image shown in the inset of (a). (c,d) Top view HRTEM image (c) and SAED pattern (d) of the Fe_3O_4 nanosheet. (e,f) Cross-sectional HRTEM image (e) and SAED pattern (f) of the Fe_3O_4 nanosheet.

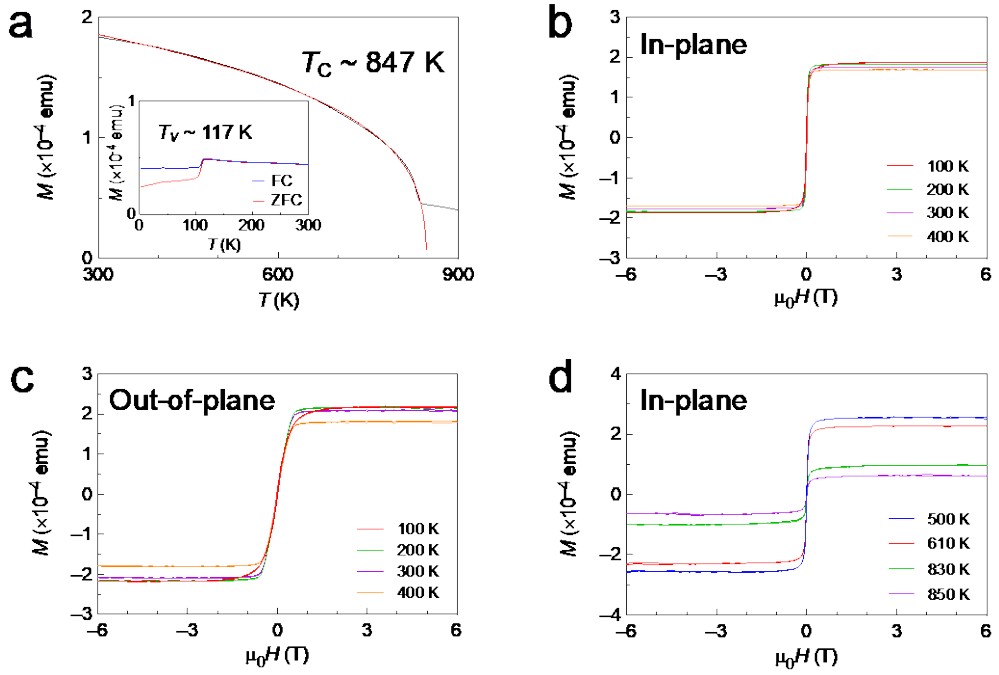

Figure 3. Magnetization characterizations of the ultrathin Fe_3O_4 nanosheets. (a) Temperature-dependent magnetization curve for the Fe_3O_4 nanosheets. The applied magnetic field is 500 Oe and parallels the surface of the Fe_3O_4 nanosheets. The T_C is extracted by fitting the curve using the Curie-Bloch equation around the phase transition: $M(T) \propto (1 - \frac{T}{T_C})^{\beta}$. Inset shows the low-temperature magnetization curve. (b,c) In-plane and out-of-plane magnetization curves at 100 to 400 K. In-plane and out-of-plane fields are applied parallel and perpendicular to the surface of the Fe_3O_4 nanosheets, respectively. (d) High-temperature in-plane magnetization curves at 500 to 850 K. The linear backgrounds in (b-d) have been subtracted.

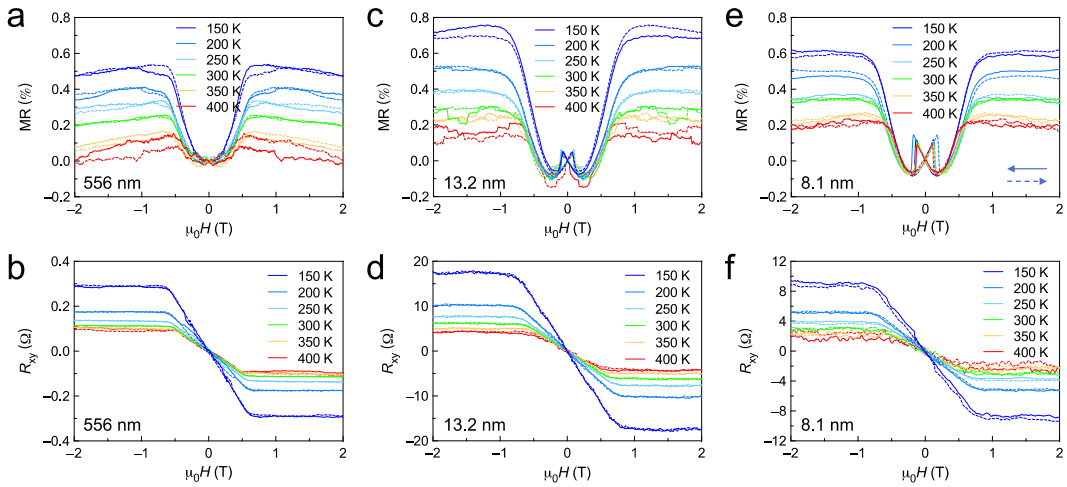

Figure 4. Magneto-transport properties of individual Fe_3O_4 nanosheets. (a,b) Out-of-plane MR (a) and the AHE (b) in a 556 nm thick Fe_3O_4 nanosheet as a function of temperature. (c,d) Out-of-plane MR (c) and the AHE (d) in a 13.2 nm thick Fe_3O_4 nanosheet as a function of time. (e,f) Out-of-plane MR (e) and the AHE (f) in an 8.1 nm Fe_3O_4 thick nanosheet as a function of temperature. The arrows in (e) represent the field sweep direction for all the devices.

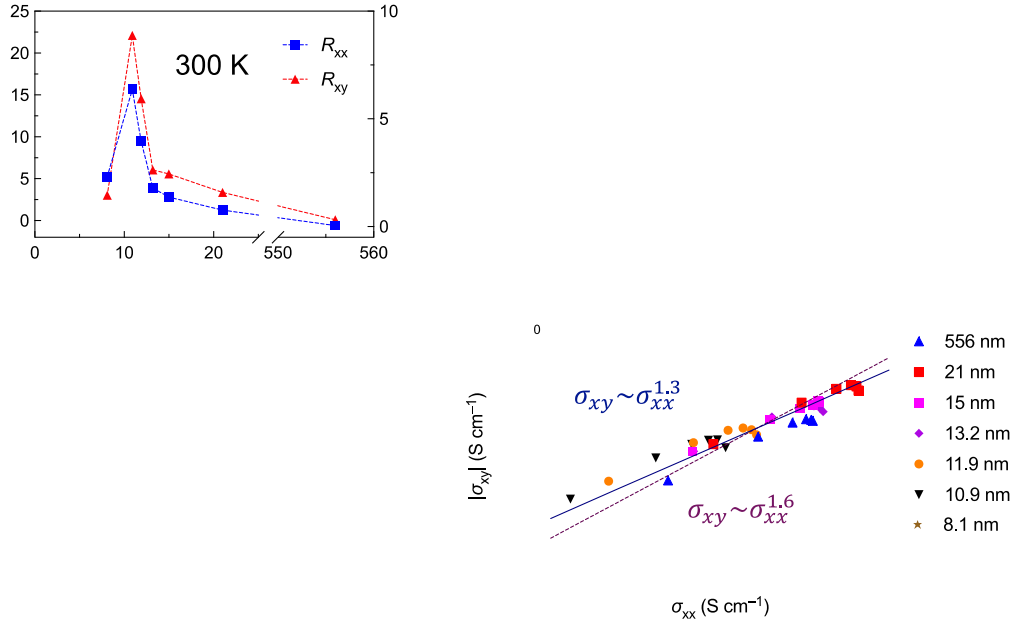

Figure 5. Relationship between the anomalous Hall resistance (conductance) and longitudinal resistance (conductance) in the Fe_3O_4 nanosheets. (a) The thickness-dependent anomalous Hall resistance and longitudinal resistance in the Fe_3O_4 nanosheets at 300 K. (b) The temperature-dependent anomalous Hall resistance and longitudinal resistance of the 13.2 nm thick Fe_3O_4 nanosheet. (c) The temperature-dependent Hall angles of the Fe_3O_4 nanosheet with various thicknesses. (d) The plot of anomalous Hall conductivity as a function of longitudinal conductivity. The solid blue line and purple dash line are fitted to $\sigma_{xy} \propto \sigma_{xx}^{1.3}$, $\sigma_{xy} \propto \sigma_{xx}^{1.6}$, respectively.

Title: Van der Waals Epitaxial Growth and High-Temperature Ferrimagnetism in Ultrathin Crystalline Magnetite (Fe_3O_4) Nanosheets

Yunzhou Xue,* Hongtao Liu, Yi Zhang, Shenghuang Lin, Shu Ping Lau*

KEYWORDS: van der Waals epitaxy, magnetite, anomalous Hall effect, Curie temperature, 2D magnet

TOC figure: